Rainfall, Convection, and Latent Heating Distributions in Rapidly Intensifying Tropical Cyclones

JOSEPH P. ZAGRODNIK AND HAIYAN JIANG

Department of Earth and Environment, Florida International University, Miami, Florida

ABSTRACT

Tropical cyclone (TC) rainfall, convection, and latent heating distributions are compiled from 14 years of Tropical Rainfall Measuring Mission (TRMM) precipitation radar overpasses. The dataset of 818 Northern Hemisphere tropical storms through category 2 hurricanes is divided by future 24-h intensity change and exclusively includes storms with at least moderately favorable environmental conditions. The rapidly intensifying (RI) category is further subdivided into an initial [RI (initial)] and continuing [RI (continuing)] category based on whether the storm is near the beginning of an RI event or has already been undergoing RI for 12 or more hours prior to the TRMM overpass. TCs in each intensity change category are combined into composite diagrams orientated relative to the environmental vertical wind shear direction. Rainfall frequency, defined as the shear-relative occurrence of PR near-surface reflectivity $>20\,\mathrm{dB}Z$, is most strongly correlated with future intensity change. The rainfall frequency is also higher in RI (continuing) TCs than RI (initial). Moderate-to-deep convection and latent heating only increase significantly after RI is underway for at least 12 h in the innermost 50 km relative to the TC center. The additional precipitation in rapidly intensifying TCs is composed primarily of a mixture of weak convective and stratiform rain, especially in the upshear quadrants. The rainfall frequency and latent heating distributions are more symmetric near the onset of RI and continue to become more symmetric as RI continues and the rainfall coverage expands upshear. The relationship between rainfall distributions and future TC intensity highlights the potential of 37-GHz satellite imagery to improve real-time intensity forecasting.

1. Introduction

Rapid intensification (RI) remains one of the most challenging aspects of tropical cyclone intensity forecasting. Many aspects of RI are uncertain, including the conditions and dynamics responsible for the beginning, ending, and magnitude of the intensification period. It is well known that RI rarely occurs without favorable environmental conditions including warm sea surface temperatures (SSTs), moisture in the low to midtroposphere, and light vertical wind shear (Kaplan and DeMaria 2003). The ability of environmental conditions to aid in RI forecasts has led to the development of the Statistical Hurricane Intensity Prediction Scheme RI index (SHIPS RI; Kaplan and DeMaria 2003; Kaplan et al. 2010). While the SHIPS RI forecasts have been shown to be skillful

(Kaplan et al. 2010), the false alarm ratio remains undesirably high. A primary reason is that favorable environmental conditions are not unique to rapidly intensifying storms and are often present during slow intensification (Hendricks et al. 2010). More information is needed about the storm's internal structure and dynamics to pinpoint the exact onset, duration, and magnitude of the RI event.

Kieper and Jiang (2012) showed that the SHIPS RI probability of detection (POD) and false alarm ratio (FAR) can be improved by supplementing the statistical forecast with a subjectively defined precipitative ring feature on the Naval Research Laboratory (NRL) 37-GHz color composite microwave satellite product (Lee et al. 2002). The NRL developed the 37-GHz color image for real-time analysis by combining the 37-GHz horizontally polarized (37H), vertically polarized (37V), and polarization-corrected brightness temperature (37PCT; Cecil et al. 2002) into a red (37PCT), green (37H), and blue (37V) color composite that qualitatively differentiates between the ocean surface (green), low-level

clouds and liquid hydrometers (cyan), and ice scattering frozen hydrometers within deep convection (pink). Kieper and Jiang (2012)'s method only works with the 37-GHz color imagery because the ring features that develop prior to RI are composed of both liquid-only precipitation (cyan) and stratiform or convective precipitation extending well above the freezing layer (pink). Detailed quantitative information regarding the precipitative ring remains limited at this time, but the effectiveness of the 37-GHz ring forecast method likely emanates from its ability to consider not only deep, mature convection, but also young and/or shallow convection in the inner core near the tropical cyclone (TC) center. More commonly used products such as infrared satellite imagery or 85-GHz polarization-corrected brightness temperature (PCT; Spencer et al. 1989) are most sensitive to frozen hydrometers, which do not leave a strong signature in precipitation below the freezing level.

Convective-scale processes within the inner core are an essential contributor to TC intensity changes. Recent studies suggest that the TC vortex intensifies as a symmetric response to the azimuthally averaged latent heat release within convection (Nolan and Grasso 2003; Nolan et al. 2007), which is most efficient when the heating is near or within the radius of maximum winds (RMW; Schubert and Hack 1982; Vigh and Schubert 2009; Pendergrass and Willoughby 2009). Rogers et al. (2013) found evidence in airborne Doppler observations that convective bursts were preferentially located within the RMW of intensifying TCs. As a result, the distribution, duration, and organization of the convection are critical in determining if intensification will occur. In general, TC precipitation and convection is predominantly orientated with respect to the environmental vertical wind shear. For at least moderate vertical wind shear values ($\geq 5\,\mathrm{m\,s}^{-1}$), the quadrant downshear and to the left of the TC center contains the maximum wavenumber-1 rainfall asymmetry (Chen et al. 2006), greatest number of lightning strikes (Corbosiero and Molinari 2003), and is characterized by a mature mixture of intense convective and stratiform precipitation (Hence and Houze 2011).

Several case studies have considered the convection for the specific case of TCs undergoing RI. A mesoscale model simulation of the Hurricane Dennis (2005) RI event by Rogers (2010) found that the onset of RI coincided with an increase in convective precipitation coverage in the inner core, especially within the RMW. Notably, RI was most directly linked with the areal coverage of weak updrafts as opposed to the strong updrafts found in deep convective bursts. Rapid intensification has also been documented in storms with moderate-to-high vertical wind shear (Reasor et al. 2009; Molinari and Vollaro 2010; Nguyen and Molinari 2012), as shear can force convergence and convective cell development in the downshear-left quadrant and within the RMW. The high-shear cases illustrate that RI is possible if convection is intense and/or persistent within the RMW, whereas sporadic convection tends to result in temporary intensification or weakening. Environmental factors such as the presence of an upper-level trough (Molinari et al. 2006) or warm SSTs (Nguyen and Molinari 2012) may help maintain asymmetric convection and reduce the influence of negatively buoyant downdrafts (Molinari et al. 2013).

Increased convection and precipitation coverage has also been linked to RI using large satellite observational datasets. Using 85-GHz brightness temperatures, Cecil and Zipser (1999) found a positive correlation between future intensity change and the spatial coverage of at least moderate rain rates. Jiang (2012) found that several parameters relating to inner-core convection were more intense in RI storms than non-RI storms. It was further determined that RI requires a minimum threshold for inner-core raining area and volumetric rain that is appreciably higher than non-RI storms (Jiang and Ramirez 2013). It is important to note that these studies do not consider environmental conditions such as wind shear and SST, which leaves a degree of uncertainty about how much of the difference in rainfall and convection between RI and non-RI storms is simply a reflection of their environment. In this study, we focus specifically on the rainfall and convection by exclusively using TCs that meet reasonable minimum environmental criteria for RI. We also consider the inner core in more detail by considering the distribution of convection relative to the TC center and relative to the vertical wind shear. Our primary goal is to develop a comprehensive description of the differences in rainfall and convection distributions between storms that do not undergo RI, those near the beginning of RI, and those that are in the middle of an RI event.

Our analysis is further aided by utilizing satellite-derived latent heating estimates. The Tropical Rainfall Measuring Mission (TRMM) spectral latent heating (SLH) algorithm (Shige et al. 2004, 2007) matches the precipitation radar (PR) vertical reflectivity profile to a corresponding latent heating profile via a lookup table derived from cloud-resolving model (CRM) simulations. The SLH algorithm was intended to be used on larger spatial and temporal time scales than instantaneous overpasses of TCs, as the simulated latent heat (LH) profiles represent the average simulated heating profile for a particular reflectivity profile. The latent heating profiles generally compare favorably to observations,

although the use of an averaged heating value below the freezing level in convective profiles results in the SLH algorithm significantly underestimating convective-scale cooling rates in tropical mesoscale convective systems (Park and Elsberry 2013). As a result, the LH results in this study likely overestimate the heating rates at lower levels in convective pixels. Nevertheless, the latent heating results are still useful for estimating the location and magnitude of the LH release and whether the LH is released from primarily convective or stratiform precipitation.

2. Data

a. TRMM overpass selection

The dataset for this study is derived from 14 years of TRMM PR (Kummerow et al. 1998) overpasses from 1998 to 2011 interpolated with global TC best-track information from the TRMM Tropical Cyclone Precipitation Feature (TCPF) database (Jiang et al. 2011). The PR has a narrow 247-km swath (215 km before August 2001 orbital boost), resulting in fewer good observations of TC inner cores and a smaller portion of each TC sampled compared with passive microwave imagery by the TRMM Microwave Imager (TMI). All overpasses in this study are manually filtered so that at least some portion of the TC center or near-center area is within the PR swath. Similar to Hence and Houze (2011), we also manually adjust the best-track TC center when the PR or TMI 37-GHz data suggest the center should be moved. The center is almost always adjusted in hurricanes with well-defined eyewalls; in tropical storms, the center is only moved if there is convincing evidence to relocate it.

Geographically, overpasses are restricted to the Northern Hemisphere, including the Atlantic, North Pacific (eastern and western), and north Indian Ocean basins. The ability to group overpasses by basin is limited by the rare occurrence of rapidly intensifying storms. Comparing the available data does indicate that the differences between basins are subtle and this study's major conclusions are likely valid for each basin individually. A related study will address the same topic using TMI overpasses divided by basin. We use version 7 of the PR 2A25 algorithm reflectivity and 2H25 latent heating data. The reflectivity has a 250-m vertical resolution and the latent heating has a 1-km vertical resolution (0.5 km at the lowest two levels). The horizontal resolution of both products is approximately $4 \times 4 \, km^2$ before boost and $5 \times 5 \, km^2$ after boost. Latent heating is closely correlated with PR 2A25 rain rates, as the linear correlation coefficient in this study is 0.89 overall and 0.74 for rain rates above $20 \, mm \, h^{-1}$. In general,

a $1 \, mm \, h^{-1}$ increase in rain rate results in a $3.5 \, K \, h^{-1}$ increase in vertically integrated LH.

The environmental criteria are added to the TRMM database from two additional datasets. The SST is derived from the 0.25°-resolution Reynolds daily SST grid point nearest to the TC center (Reynolds et al. 2007). The total precipitable water (TPW) and wind shear data are derived from the Interim European Centre for Medium-Range Weather Forecasting (ECMWF) Re-Analysis dataset (Simmons et al. 2006). We use the time (6 hourly) nearest to the TRMM overpass. The 0.75°-resolution TPW data was averaged for the innermost 250 km around the TC center. The vertical wind shear is computed following the method of Hence and Houze (2011) by averaging the 200- and 850-hPa wind vectors between 500 and 750 km from the storm center. The vertical wind shear magnitude and direction is the difference between the average vectors at the two levels. The storm motion is interpolated from the two best-track center locations closest to the time of the TRMM overpass.

b. Selection of intensity change and environmental criteria

All overpasses are divided into five categories based on the difference in intensity (defined as the maximum surface sustained wind) between the time of the TRMM overpass and 24 h in the future. Table 1 contains the definitions and final sample sizes in the four Northern Hemisphere basins. Previous related studies (Jiang 2012; Jiang and Ramirez 2013) have four intensity change categories: weakening (W), neutral (N), slowly intensifying (SI), and RI. The extra category comes from dividing the RI category into two subcategories. Rapid intensification events often continue for multiple 24-h periods, so it is important to distinguish between overpasses near the onset of RI and those in which RI is already ongoing. Similar to Kieper and Jiang (2012), this study considers an RI event as a sequence of continuous and overlapping 24-h periods in which the intensity increased in each period by 30 kt (1 kt $\approx$ 0.51 m s^{-1}) or more. The RI periods are defined in 6-h increments relative to the TRMM overpass time using best-track data interpolated from the nearest synoptic times (Jiang et al. 2011). Storms designed as RI (initial) began an RI event within 12 h of the overpass, while RI (continuing) contains the storms that had a previous 24-h RI period beginning at 12, 18, or 24 h prior to the overpass. The RI event in both subcategories continues for at least 24 h following the overpass as well.

The sample sizes do not represent the full spectrum of TRMM TC overpasses but instead are restricted by several important criteria. First, the initial maximum

TABLE 1. Definition of intensity change categories and the total sample (after removing unfavorable environmental conditions) in the full Northern Hemisphere sample and divided by four basins: Atlantic (ATL), east-central Pacific (EPA), northwest Pacific (NWP), and north Indian Ocean (NIO). Here $V_{max}(t)$ is defined as the maximum sustained wind in knots and t is the time in hours relative to the TRMM overpass.

Intensity change	Definition	Total NH	ATL	EPA	NWP	NIO
W	$V_{max}(+24) - V_{max}(0) < -10\,kt$	136	30	35	63	8
N	$-10 \leq V_{max}(+24) - V_{max}(0) < 10\,kt$	329	90	71	151	17
SI	$10 \leq V_{max}(+24) - V_{max}(0) < 30\,kt$	250	49	52	136	13
RI (initial)	$V_{max}(+24) - V_{max}(0) \geq 30\,kt$ and $V_{max}(0, +6, +12) - V_{max}(-24, -18, -12) < 30\,kt$	49	10	11	28	0
RI (continuing)	$V_{max}(+24) - V_{max}(0) \geq 30\,kt$ and $V_{max}(0, +6, +12) - V_{max}(-24, -18, -12) \geq 30\,kt$	54	11	11	30	2
Total	—	818	190	180	408	40

sustained wind at the time of the overpass must be between 33 and 95 kt or tropical storm through category 2 hurricane intensity. Tropical depressions are not included because they represent only a small portion of RI cases (Kaplan et al. 2010). Category 3–5 hurricanes are not included because they often intensify and weaken through eyewall replacement cycles (Willoughby et al. 1982), which should be considered in separate studies. In addition, this study is restricted to only include TCs that are under favorable environmental conditions at the initial overpass time. Hendricks et al. (2010) concluded that internal dynamical processes mostly control rapid intensification, provided that a favorable environment exists. Removing TCs under unfavorable environmental conditions allows us to emphasize the role of rainfall, convection, and latent heating distributions in predicting future intensity change under the presence of a favorable or at least semifavorable environment. The probability of RI is higher when environmental conditions are well above the minimum criteria (Kaplan et al. 2010), but setting a minimum restriction at least removes unfavorable environmental conditions as an explanation for the differences between intensity change categories in this study.

Figure 1 displays the frequency distributions of SST, TPW, storm motion, and 850–200-hPa environmental wind shear magnitude of all PR overpasses considered for this study (with land interaction already excluded). The full distribution is divided by five colors into the W, N, SI, and RI (initial) and RI (continuing) subsets. The light shaded section represents the storms removed for falling outside of the environmental condition criteria: SST $> 26°C$, mean inner 250-km TPW $> 50\,mm$, vertical wind shear $< 16\,m\,s^{-1}$, and storm motion $< 11\,m\,s^{-1}$. The cutoff criteria are derived from a larger dataset of several thousand TRMM overpasses that includes all TC centers within the TMI swath. All storms that underwent RI in that larger dataset had environmental conditions that met or exceeded these minimum criteria. These criteria are not quite necessary conditions, as RI can occasionally occur with an SST below 26°C (Kaplan and DeMaria 2003). However, they do eliminate storms with highly unfavorable conditions in which RI had almost no probability of occurring. With the unfavorable environmental conditions removed, the remaining dataset has similar distributions of environmental conditions, as shown in Table 2. There is a statistically significant difference in wind shear between RI (initial) and RI (continuing) at a 95% confidence level, but the mean difference is only $1.3\,m\,s^{-1}$. The difficulty of predicting the onset of RI based on the environment alone is illustrated by the nearly identical distributions between SI and RI (initial). Even the RI (continuing) category is not remarkably different.

The initial intensity distribution for the final dataset is shown in Fig. 2a. Weakening and RI (continuing) storms have the highest initial intensities, but all categories are distributed across the spectrum of initial intensities. Figure 2b shows the intensity change in the 12 h prior to the TRMM overpass. As demonstrated in Kaplan and DeMaria (2003) and Kaplan et al. (2010), TCs at the onset of RI are typically intensifying at a faster rate in the previous 12 h than non-RI storms. The RI (continuing) storms have high previous-12-h intensity rates by definition. Figure 3 illustrates the mean time series of intensity change in the 48 h surrounding the overpass. Some storms had not yet formed at −24 h and are not included in the averages at the times in which they did not have an intensity value (mostly in the N and SI categories). Slowly intensifying and RI (initial) storms are nearly identical leading up to the time of the TRMM overpass, but they diverge to a mean difference of 21 kt at +24 h. The RI (continuing) category is 14 kt higher than RI (initial) at the overpass time and gains an additional 10 kt more than RI (initial) in the 24 h after the overpass.
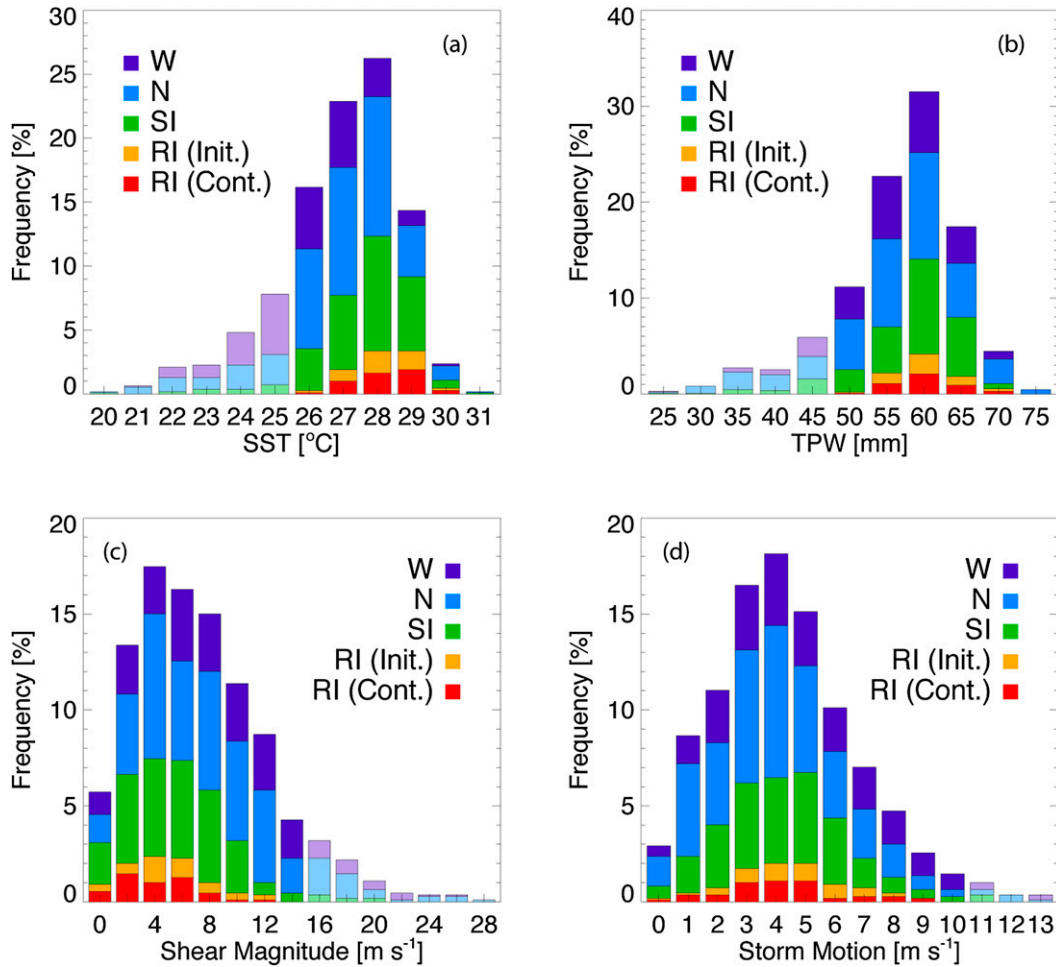
FIG. 1. Frequency distribution of environmental conditions: (a) SST, (b) TPW, (c) shear magnitude, and (d) storm motion. Each distribution is divided into colors representing the five future 24-h intensity change categories. The faded bars represent the section of the distribution that is removed because conditions are unfavorable for RI.

c. Image generation and variable selection

This study uses several types of figures: radial distributions, composite images, radial–height diagrams, contoured frequency by altitude diagrams (CFADs; Yuter and Houze 1995), and scatterplots. The radial distribution plots are generated by grouping the PR pixels from the five intensity change categories into bins representing 5-km annuli extending radially outward from the TC center. The radial–height distributions include the vertical information and are further divided into the four shear-relative quadrants. The composite images are generated by first rotating the PR overpasses to orient the vertical wind shear direction upward along the $+y$ axis. Figure 4 shows the variation in the wind shear magnitude and direction for the four intensity change categories. The shear direction generally follows the climatological norms (westerly in the Atlantic and

east-northeasterly in the eastern North Pacific), but shear from all directions is observed in most areas. The new shear-relative PR pixels are then compiled into $10 \times 10 \, \text{km}^2$ grid cells with the TC center in the middle. The value of each grid cell represents the frequency of pixels

TABLE 2. Mean values of SST, TPW, shear, and storm motion parameters for the total dataset and the four intensity change categories. The storms with unfavorable environmental conditions are removed from these data (light shaded columns in Fig. 1).

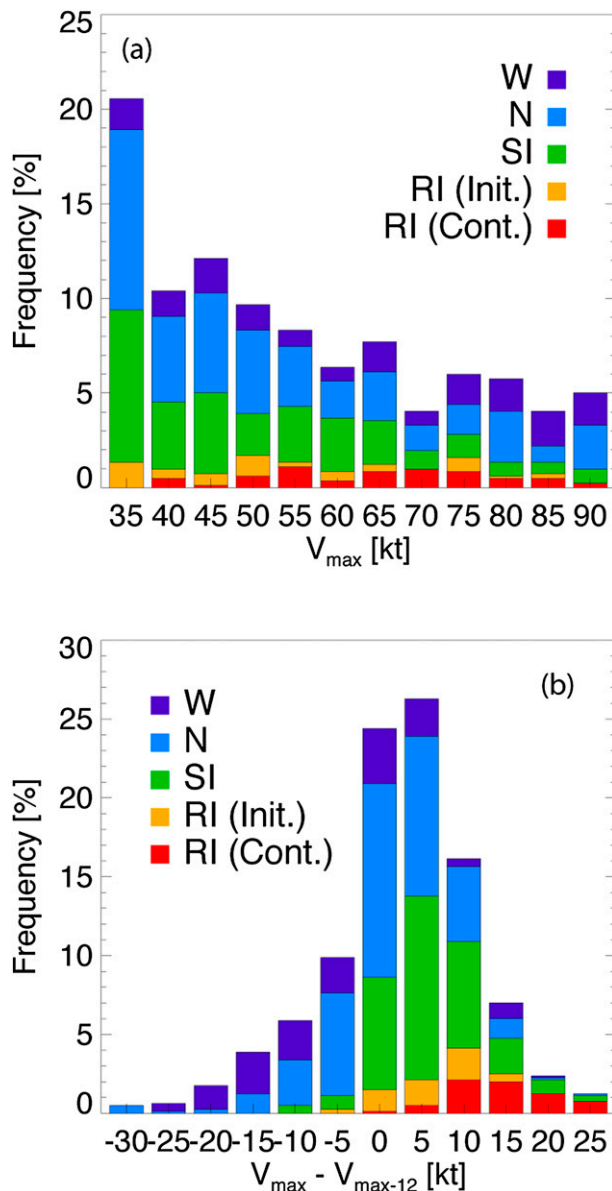| Intensity change	SST (°C)	TPW (mm)	Shear (m s^{-1})	Motion (m s^{-1})
W	27.5	60.7	8.5	4.9
N	28.0	61.6	7.7	4.4
SI	28.4	62.4	6.4	4.7
RI (initial)	28.6	62.6	6.3	5.1
RI (continuing)	28.7	62.8	5.0	4.7
All	28.1	61.8	7.2	4.6

FIG. 2. Frequency distribution of (a) maximum surface sustained wind speed intensity (V_{max}) at the time of the TRMM overpass and (b) the change of V_{max} during the previous 12 h before the overpass. This figure contains the final sample with only storms that meet the specified environmental criteria from Fig. 1.

satisfying the designated criteria (explained in the next paragraph) relative to all pixels that fall into each $100 \, \text{km}^2$ box. The PR swath is too narrow to cover the full grid domain, but since the PR sample is restricted to storms with at least partial coverage of the near-center area, the swath coverage is highest near the center of the composites and decreases outward with increasing radius. One limitation of the composite images is that they do not contain any information about the behavior of individual storms. Information about the variance in the dataset can

be inferred by making scatterplots with a single value for each storm's full inner-75-km rainfall or convection frequency. However, the scatterplot dataset has to be further restricted to remove overpasses that only partially observe the TC inner core. Therefore, the sample size for Tables 3 and 4 (shown in Fig. 13) is reduced by a third from 818 to 559.

Rainfall, convection, and latent heating are analyzed using four primary variables from the TRMM reflectivity and LH information. The rainfall coverage is inferred from the frequency of PR pixels with a near-surface reflectivity exceeding 20 dBZ. The frequency of >20-dBZ pixels is simply the fraction of >20-dBZ near-surface reflectivity pixels divided by the total number of PR pixels in the selected annulus or gridded domain. The 20-dBZ level is selected because it is closely analogous to the raining area and was used to define precipitation features in Nesbitt et al. (2000). We select the percentage occurrence of >40-dBZ pixels as a moderate-to-heavy rain threshold. To assess the frequency of convection, we count the frequency of occurrence of pixels with a >20-dBZ echo above 10 km. This is a softer criterion than the 14.5-km level used for hot towers (Jiang 2012) but still limited to deep convection that reaches the upper levels of the troposphere. For convenience, we refer to the near-surface >20-dBZ reflectivity frequency as "rainfall frequency" and the 10-km >20-dBZ reflective frequency as the "frequency of moderate-to-deep convection." The latent heating (K h^{-1}) is displayed both by height (up to 15 km) and vertically integrated from the surface to 18 km. The LH is an average based on the total LH in an annulus or grid cell divided by the number of pixels in the domain. A CFAD figure is also included to assess the frequency of occurrence of radar echoes as a function of altitude and reflectivity. The CFADs in this study are analogous to the normalized TRMM CFADs in Hence and Houze (2011), except that we include the inner 75-km, upshear semicircle because we cannot distinguish between the eyewall and rainbands in weaker TCs. The CFADs are especially useful for statistical comparisons of the vertical structure of precipitation, including whether certain regions tend to contain primarily shallow/weak convective, mature convective, or stratiform rain. The scatterplots and CFADs simply use the inner 75 km because we do not have the ability to locate the RMW in weaker TCs. From the storms with near or partial eyewalls, we roughly estimate that the mean RMW is 49 km for SI and 38 km for the combined RI (initial and continuing) storms, which compares favorably with RMW values of 43 for intensifying and 53 for steady-state TCs in Rogers et al. (2013). The 75-km cutoff is enough cover at least one standard deviation from the
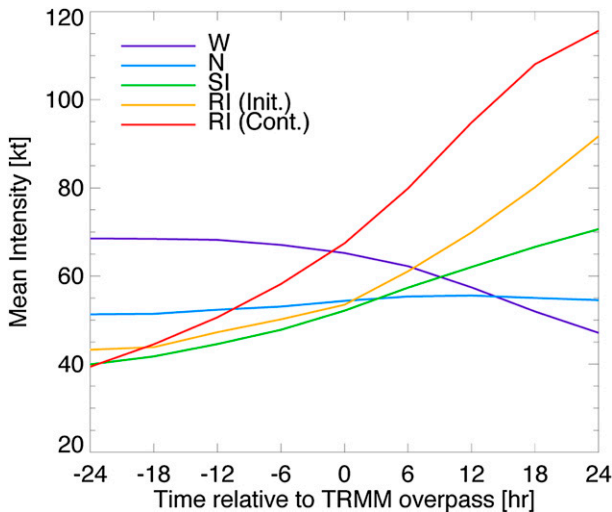
FIG. 3. Mean intensity evolution of the five intensity change categories from 24 h prior to the TRMM overpass through 24 h after.

estimated mean RMW, but some of the noise in the scatterplots and CFADs is likely caused by the broad inner-region definition.

3. Results

a. Radial distributions

Before considering the shear-relative distributions, we first examine the radial frequency of rainfall and convection in Fig. 5. Figure 5a shows that the frequency of near-surface reflectivity exceeding 20 dBZ is much higher for both rapidly intensifying categories. Rapidly intensifying storms also have their peak radius of >20-dBZ coverage closer to the center than other categories, mostly likely because their mean RMW is closer to the TC center. The 40–45-km annulus is greatest for RI (initial and continuing) while SI, N, and W storms have peak coverage at 55–60, 60–65, and 65–70 km, respectively. There is little difference in >20-dBZ coverage beyond 150 km, so the increase in raining coverage before RI is confined to the inner core and inner rainbands. The percentage coverage of >40-dBZ reflectivity in Fig. 5b indicates that on average, moderate-to-heavy rainfall is significantly more widespread in storms that are continuing rapid intensification. Slowly intensifying and RI (initial) storms are both near the black curve that represents the full 818 TC sample.

A similar pattern is observed for the moderate-to-deep convective parameter (10-km reflectivity >20 dBZ) and vertically integrated latent heating. The peak of the RI (continuing) curve is around double the rest of the categories, but it is only greater in the 20–50-km

range from the TC center. In Fig. 5c, the frequency of moderate-to-deep convection actually drops below the other categories beyond 60 km, indicative of convection concentrating near the center and outflow suppressing deep convection at upper levels in the inner-band region (Hence and Houze 2012). Overall, Fig. 5 demonstrates that rainfall frequency is the only parameter that has appreciable differences in SI, RI (initial), and RI (continuing) TCs. This result is consistent with the modeling simulation of Hurricane Dennis in Rogers (2010) and will be explored further throughout this study. The other categories show minimal difference between SI and RI (initial), which illustrates the difficulty of anticipating RI from parameters that are more closely related to the intensity of convection. Another important observation from Fig. 4 is that W and N storms all have very similar precipitation distributions. In these non-RI cases, the environmental conditions may play a more significant role in determining the future intensity change, especially in weakening and neutral storms where the environment is more likely to be marginally favorable (Table 2).

b. Composite images

The composite images in Figs. 6–9 use the same parameters as the radial plots in the previous section but allow for shear-relative analysis. The composites are oriented with the shear vector pointing upward along the +y axis and the storm center in the middle. Dotted range rings represent the 50-, 100-, 150-, and 200-km radii. Shear-relative images are described using a quadrant approach (Chen et al. 2006), with the upper-left, upper-right, lower-left, and lower-right quadrants labeled as downshear left (DL), downshear right (DR), upshear left (UL), and upshear right (UR), respectively.

1) PR NEAR-SURFACE REFLECTIVITY

Figure 6 shows the composite distribution of the frequency of PR near-surface reflectivity >20 dBZ. These shear-relative rainfall distributions are closely analogous to the wavenumber-1 rainfall asymmetry in Figs. 3 and 4 of Chen et al. (2006), as the downshear-left quadrant is favored in all cases for the greatest rainfall frequency and highest rain rates. As in Fig. 5, there is a progressive increase in rainfall frequency from N to RI (continuing). In RI (continuing) storms, the downshear-left quadrant still has the highest rainfall frequency peaking at greater than 90%, but the overall appearance is more axisymmetric with a ring of 70%–80% frequency extending completely around the center. The RI (initial) category has a gap below 50% frequency in the upshear-right quadrant. The SI composite reaches 50% frequency around about half of the center, while N and W
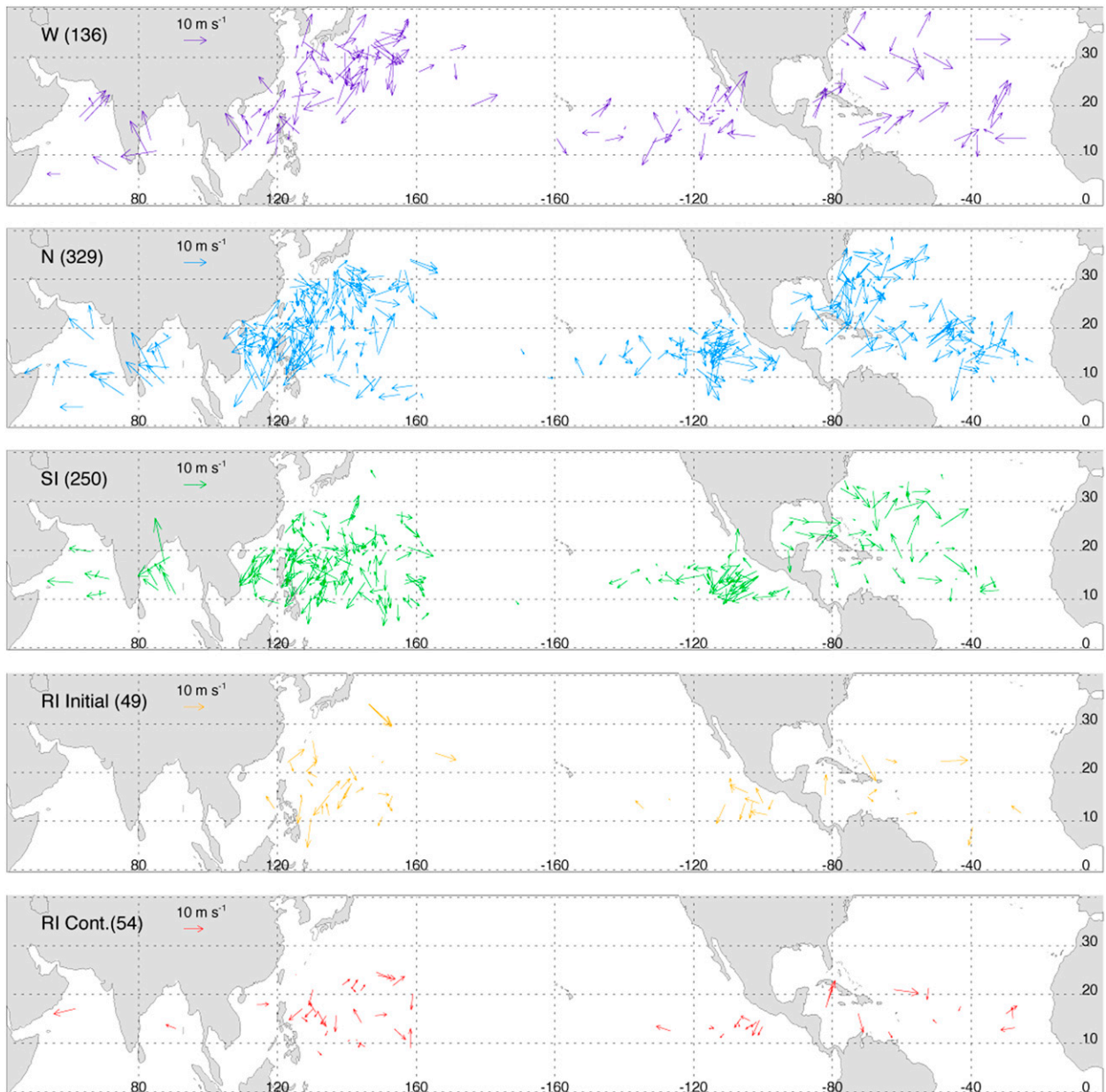
FIG. 4. Locations and vertical wind shear vectors of the storms in the final dataset, divided by intensity change category. Larger vectors represent greater vertical wind shear, relative to the $10\,\mathrm{m\,s^{-1}}$ reference vector.

have >50% frequency mostly in the downshear-left quadrant. The difference in maximum frequency between downshear left and upshear right decreases from about 50% in W to 35% in RI (initial) and 20% in RI (continuing).

Figure 7 further illustrates the progression to more axisymmetric rainfall frequency by comparing the difference in frequency between Figs. 6b and 6c, between Figs. 6c and 6d, and between Figs. 6d and 6e. Figure 7a shows a mostly uniform distribution of 5%–20% greater

rainfall frequency between SI and N storms. The differences between RI (initial) and SI and between RI (continuing) and RI (initial) in Figs. 7b and 7c have more noise because of the reduced sample sizes but both generally show the greatest differences in the upshear half. The RI (continuing) category has the most concentrated frequency increases in the innermost 50 km of the upshear-right quadrant. Rogers et al. (2013) found a similar increase in the azimuthal coverage of reflectivity for intensifying storms relative to steady-state

TABLE 3. Number of times (by shear-relative quadrant) that the inner 75-km vertically integrated latent heating is greater than any of the other three quadrants. The second column from the right depicts the percentage of the 559 storm samples that had the maximum latent heating in the downshear-left quadrant. The rightmost column contains the average ratio of total latent heating between the quadrant with the highest and lowest LH values.

Intensity change	DL	DR	UL	UR	Max LH in DL	LH ratio (max: min)
W	58	18	17	8	57.4%	18.1
N	125	33	42	17	57.6%	16.2
SI	83	38	35	12	49.4%	15.9
RI (initial)	17	9	9	3	44.7%	8.7
RI (continuing)	14	6	10	5	40.0%	4.8
All	297	104	113	45	53.1%	13.2

cases. Figures 5–7 in this study further indicate that rapidly intensifying TCs likely experience a gradual trend toward less asymmetry from the time of initial intensification through at least the early RI stages. It is worth noting that subsets of the data that include only the high ($>8 \, m \, s^{-1}$)– or the low ($<3 \, m \, s^{-1}$)–vertical wind shear storms still have the same pattern as Fig. 6, meaning that the shear-induced, asymmetric secondary circulation is likely a common feature of rapidly intensifying TCs, including those under relatively weak vertical wind shear. Reasor et al. (2013) observed that TCs with very low shear of less than $4 \, m \, s^{-1}$ had low-level inflow in the upshear quadrants and more axisymmetric reflectivity profiles than those with shear $>7 \, m \, s^{-1}$. Section 3c further explores the nature of upshear precipitation.

2) PR 10-KM REFLECTIVITY

Figure 8 shows the frequency of >20-dBZ reflectivity at or above 10 km. It is quite rare for 20-dBZ reflectivity to reach the 10-km level, as the maximum shear-relative frequency is around 12% in RI (continuing). However, the moderate-to-deep convection has a disproportionate contribution to the latent heating budget. In the inner 50 km, the pixels with 10-km reflectivity above 20 dBZ encompass 4% of the pixel count and 30% of the latent heat release. Weakening, neutral, and slowly

intensifying storms have a similar pattern as the rainfall distribution, with the downshear-left quadrant containing significantly more moderate-to-deep convection than any other quadrant. In Fig. 8d for RI (initial), the maximum frequency of reflectivity reaching 10 km shifts more toward the upshear-left quadrant, but convection is only slightly more common on the right-of-shear side of the storm. A major difference is observed in the RI (continuing) cases, as the frequency of moderate-to-deep convection is higher than RI (initial) in all four quadrants and almost entirely concentrated within the innermost 50 km, likely near or within the RMW.

Deep convection near or within the RMW has been linked to vortex strengthening in numerous studies (Vigh and Schubert 2009; Pendergrass and Willoughby 2009; Reasor et al. 2009; Sitkowski and Barnes 2009; Molinari and Vollaro 2010; Rogers 2010; Nguyen and Molinari 2012). There is likely also a connection in these results, since the RI (continuing) storms intensify by an average of 49 kt in the subsequent 24 h. However, Fig. 8 indicates that there is little difference in the frequency of moderate-to-deep convection between N, SI, and RI (initial) storms. This suggests that rapid intensification is likely triggered by other mechanisms and that the appearance of widespread deep convection is more likely a response or positive feedback to changes in the vortex that that occur earlier in the SI to beginning of RI period.

3) VERTICALLY INTEGRATED LATENT HEATING

The general pattern of the latent heating distributions in Fig. 9 is also similar to the rainfall distribution in Fig. 6. The maximum latent heating occurs in the downshear-left quadrant in all categories and RI (continuing) storms have higher latent heating values wrapped around the upshear and right-of-shear side of the center. The area of maximum latent heating is closer to the center in RI (continuing) storms than SI and RI (initial). Unlike the rainfall and convection composites, weakening storms have slightly higher downshear-left values than SI and RI

TABLE 4. Mean values of the rainfall and convective coverage within the innermost 75 km of the TC center. Asterisks following values represent the statistical significance between RI (initial) and SI at the 95% level (*), 99% level (**), and 99.9% level (***). Plus signs have an analogous meaning for the statistical significance between RI (continuing) and RI (initial).

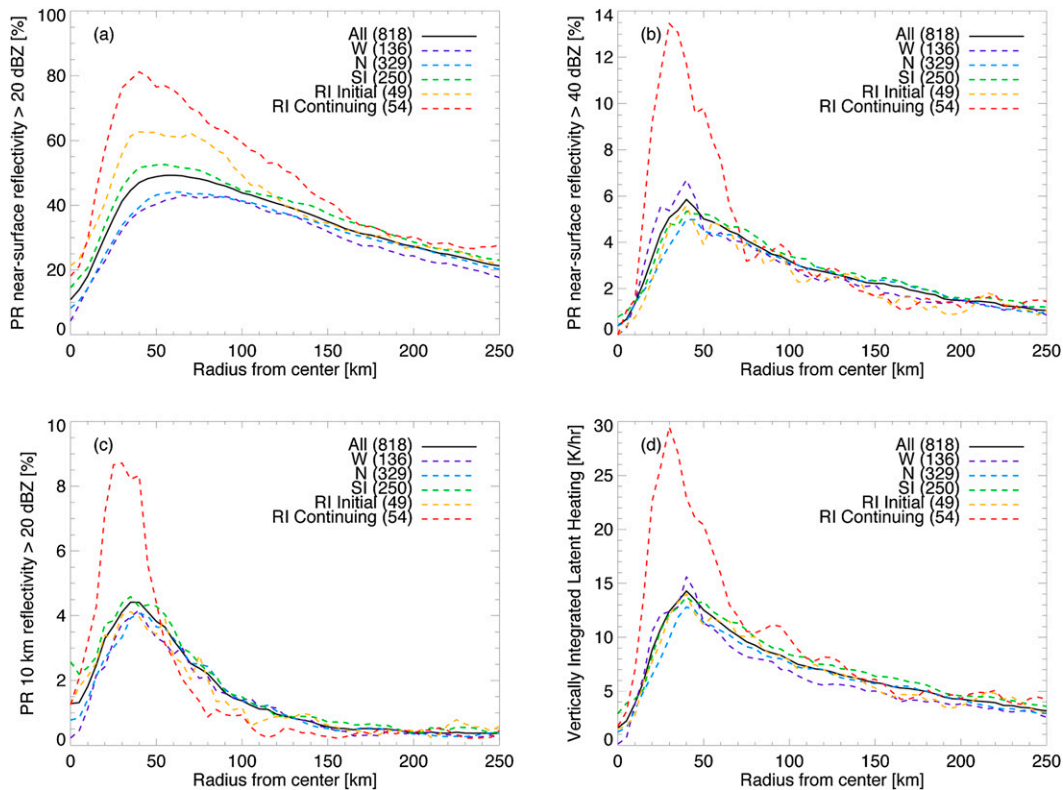| Intensity change	Near-surface dBZ >20 (%)	Near-surface dBZ >40 (%)	10-km dBZ >20 (%)	LH (K h^{-1})	Near-surface >20-dBZ asymmetry ratio	LH asymmetry ratio
W	36.8	4.9	3.3	11.0	2.0	2.6
N	39.3	4.1	3.2	10.1	2.0	2.7
SI	46.7	4.6	3.6	11.5	1.8	2.5
RI (initial)	58.5**	4.4	3.1	11.1	1.6	2.3
RI (continuing)	72.0++	8.6+++	4.4	18.5+++	1.2++	1.8+
All	44.5	4.7	3.4	11.3	1.9	2.5

FIG. 5. Line plots of the radial variation (a)–(c) rainfall and (d) convective parameters from 5-km annuli, organized by the total sample (black solid line) and the intensity change categories (colored dashed lines).

(initial) storms. From Fig. 3, the higher initial intensity of weakening storms compared with N, SI, and RI (initial) may partially explain the high downshear-left weakening LH value. The RI (initial) category does not have as strong of a downshear-left maximum as SI, as more LH is spread around to the downshear-right and upshear-left quadrants.

While the average latent heating is clearly greatest in the downshear-left quadrant, the composites average all storms and do not show the variability within the dataset. It is also important to know (on a storm by storm basis) how often the maximum heating is downshear left. This cannot be answered for partial overpasses, but it can be done for the 559 storms with at least two-thirds coverage of the inner 75 km. Table 3 shows that 297 of the 559 storms (53%) have maximum inner-core latent heating in the downshear-left quadrant.[1] Only 45 storms (8%) have the LH maximum in the upshear-right quadrant. The other 39% of cases are nearly equally divided between the downshear-right and upshear-left quadrants. Weak vertical wind shear or a combination of

storm motion and vertical wind shear likely explains why about half of the storms have maximum latent heating outside of the downshear-left quadrant, but even in those cases the latent heating distributions are still usually asymmetric. Storms in both RI categories are also much more likely to have their maximum LH downshear left compared with upshear right. However, the RI storms do have a smaller difference between the quadrants with the highest and lowest values of latent heating. The latent heating ratio of the maximum to minimum quadrant is 13.2 overall, 8.7 for RI (initial), and 4.8 for RI (continuing). The RI storms still have asymmetric inner cores, but they are much less asymmetric than any other intensity change category, including SI. This suggests that although the downshear-left precipitation is a common feature in TCs, the development of rainfall and convection in other quadrants is especially important to future intensity change.

c. Upshear reflectivity CFADs

To further illustrate the vertical structure and composition of upshear precipitation, reflectivity CFADs are displayed in Fig. 10 for the inner 75-km, upshear semicircle of the five intensity change categories. The CFADs are normalized relative to their respective

---

[1] The statistics for rainfall coverage are nearly identical to LH: 52% of all cases have maximum rainfall coverage downshear left.
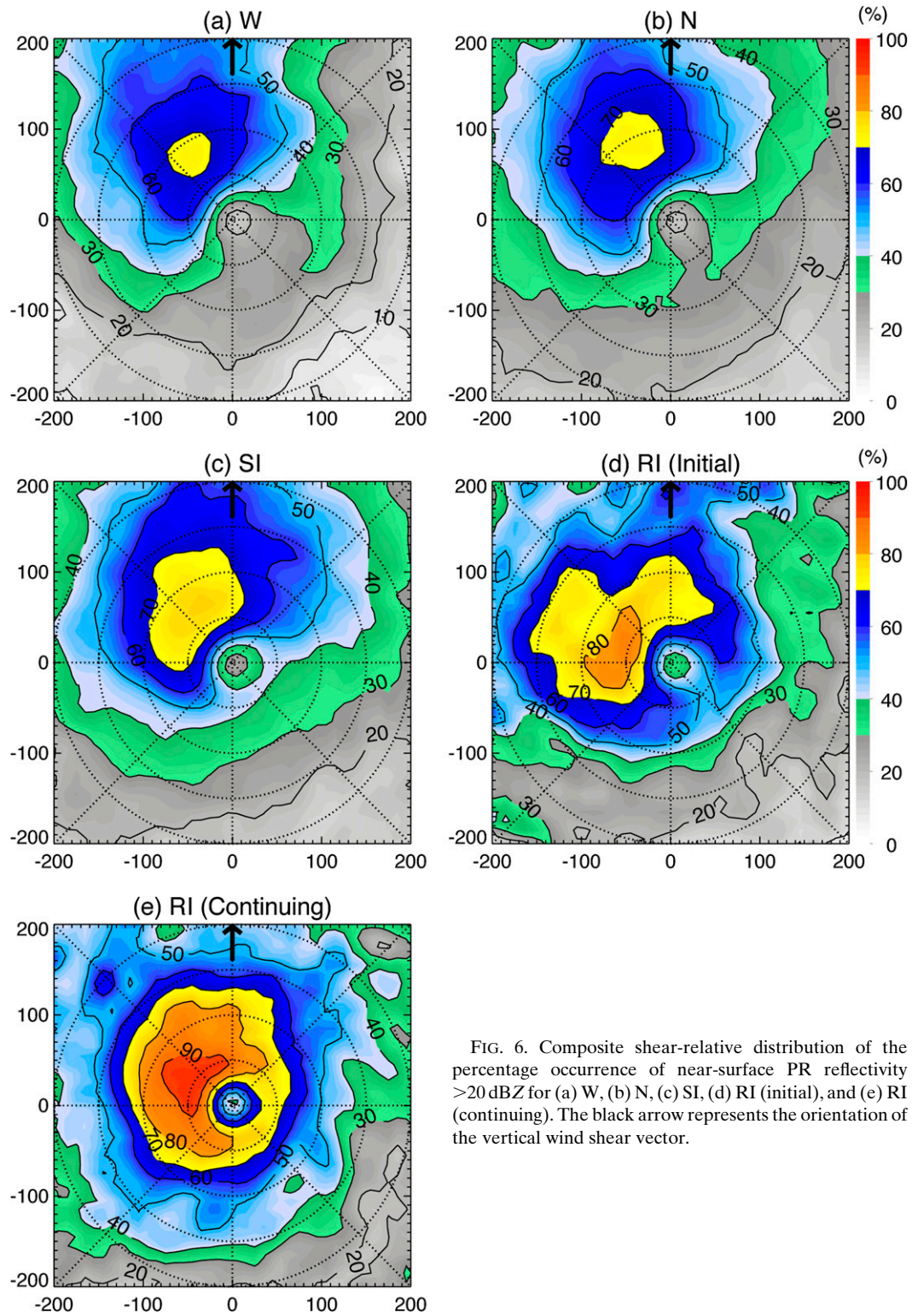
FIG. 6. Composite shear-relative distribution of the percentage occurrence of near-surface PR reflectivity $>20\,dBZ$ for (a) W, (b) N, (c) SI, (d) RI (initial), and (e) RI (continuing). The black arrow represents the orientation of the vertical wind shear vector.
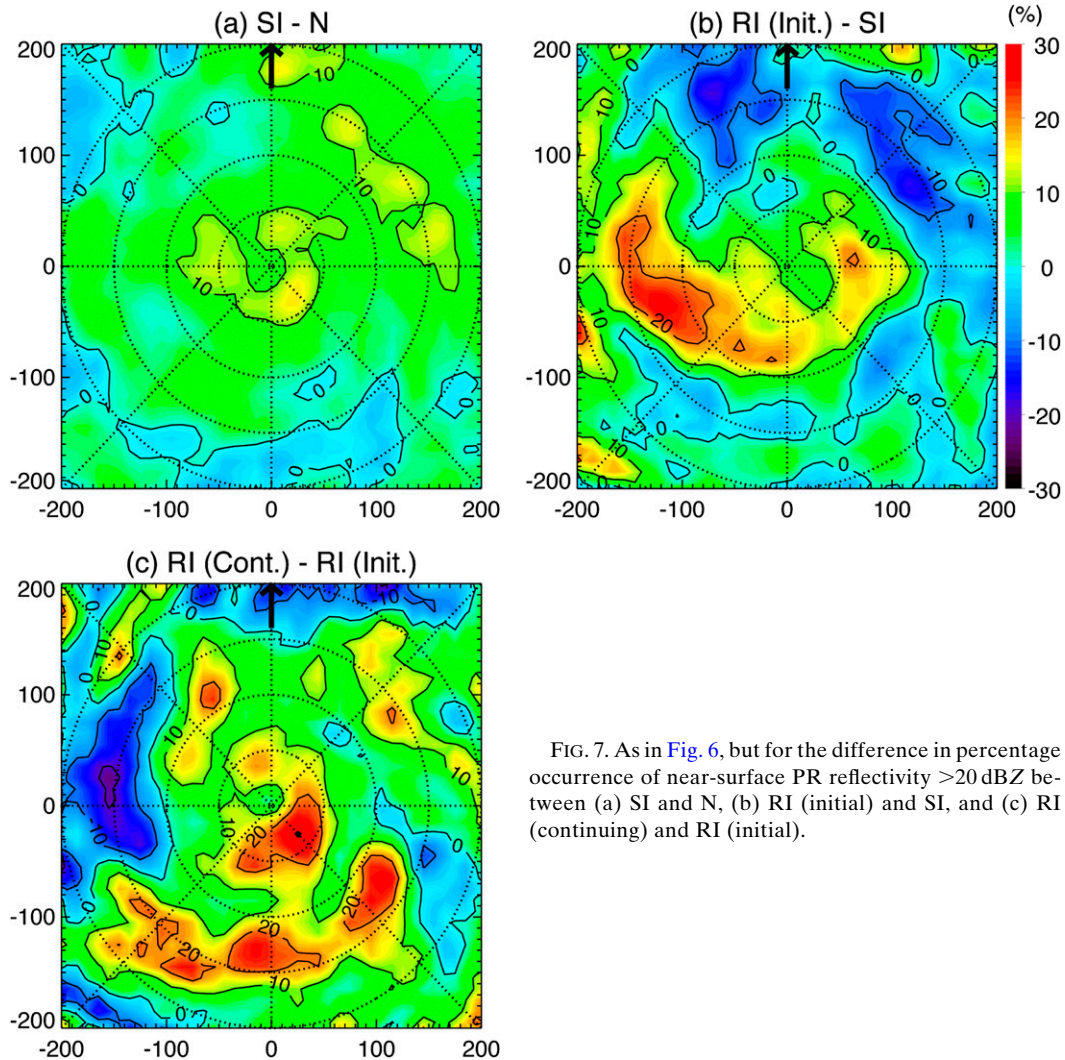
FIG. 7. As in Fig. 6, but for the difference in percentage occurrence of near-surface PR reflectivity >20 dBZ between (a) SI and N, (b) RI (initial) and SI, and (c) RI (continuing) and RI (initial).

maximum frequency to account for different sample sizes, as in Hence and Houze (2011, 2012). We also follow their convention in referring to the >50% (dark blue) frequency as the modal distribution. Figure 10f contains the outline of the PR 2A23 (Awaka et al. 2009) convective and stratiform CFADs for reference. The broad modal distribution below the freezing level in W and N storms most closely resembles the stratiform distribution in Fig. 10f. The outlier distribution above the freezing level extends higher than what would be expected from a purely stratiform CFAD, which is indicative of at least some deeper convection that is most likely advected cyclonically from the downshear-left quadrant (Reasor et al. 2013; DeHart et al. 2014). The SI, RI (initial), and especially the RI (continuing) modal distributions are shifted toward higher reflectivities below the freezing level, centered around 30–35 dBZ. These distributions do not contain the higher percentages of

35–45-dBZ reflectivities below the freezing level that would be expected in strong convective or eyewall CFADs. Instead, the upshear RI CFADs are clearly dominated by a mixture of weak convective and stratiform rain as opposed to deep and intense convection. Although deep convection reaching above 10 km is more numerous upshear in the RI (continuing) composite in Fig. 8, the majority of the increase in upshear precipitation is from less intense convection and moderate-to-strong stratiform precipitation. These CFADs are consistent with the findings from Rogers (2010) and Rogers et al. (2013) that weak updrafts are most closely linked with RI and accomplish a greater portion of the mass flux compared with intense convection.

d. Radial–height LH diagrams

The radial and vertical distribution of latent heating for RI (initial) storms is shown in Fig. 11 and the same
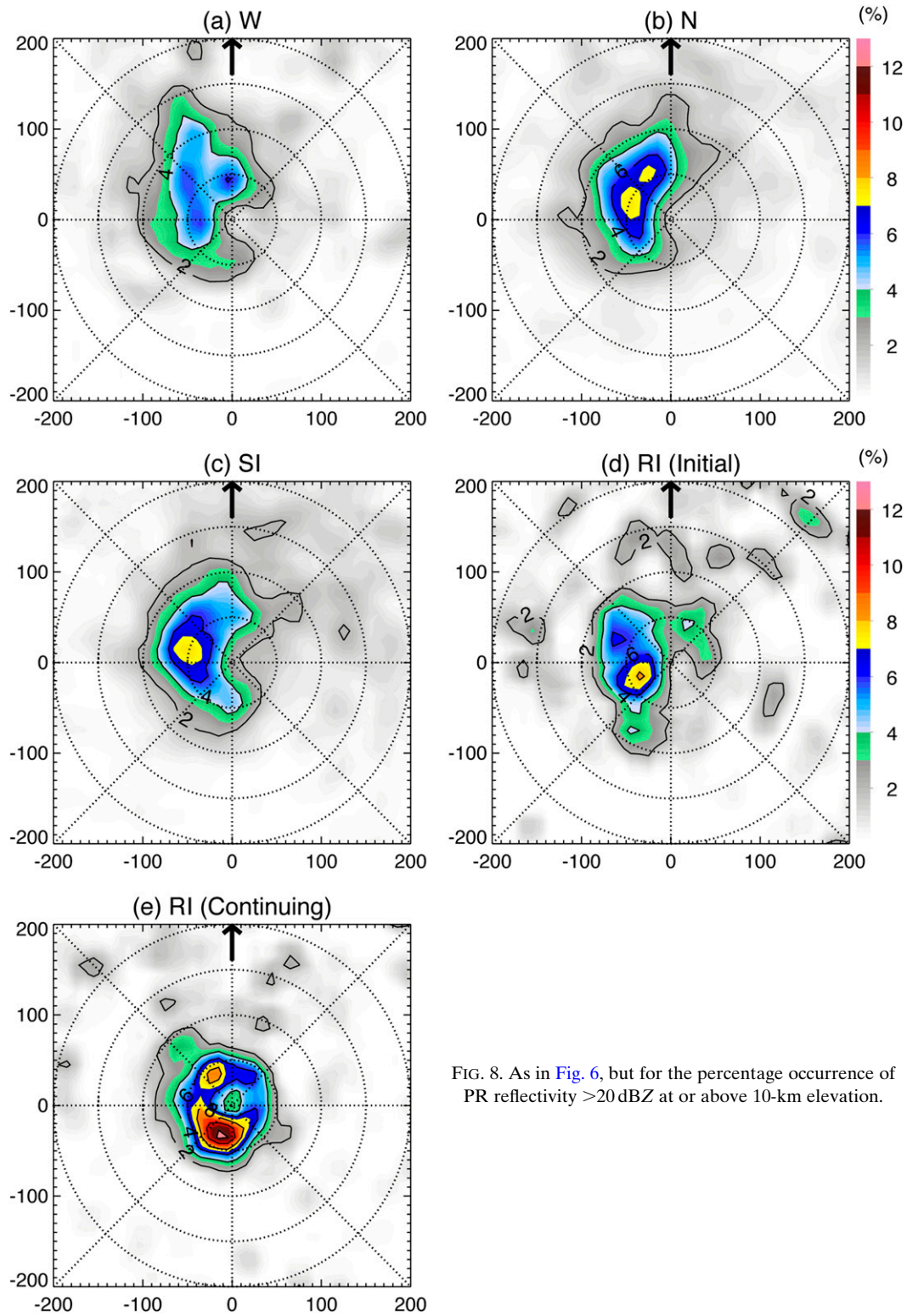
FIG. 8. As in Fig. 6, but for the percentage occurrence of PR reflectivity >20 dBZ at or above 10-km elevation.
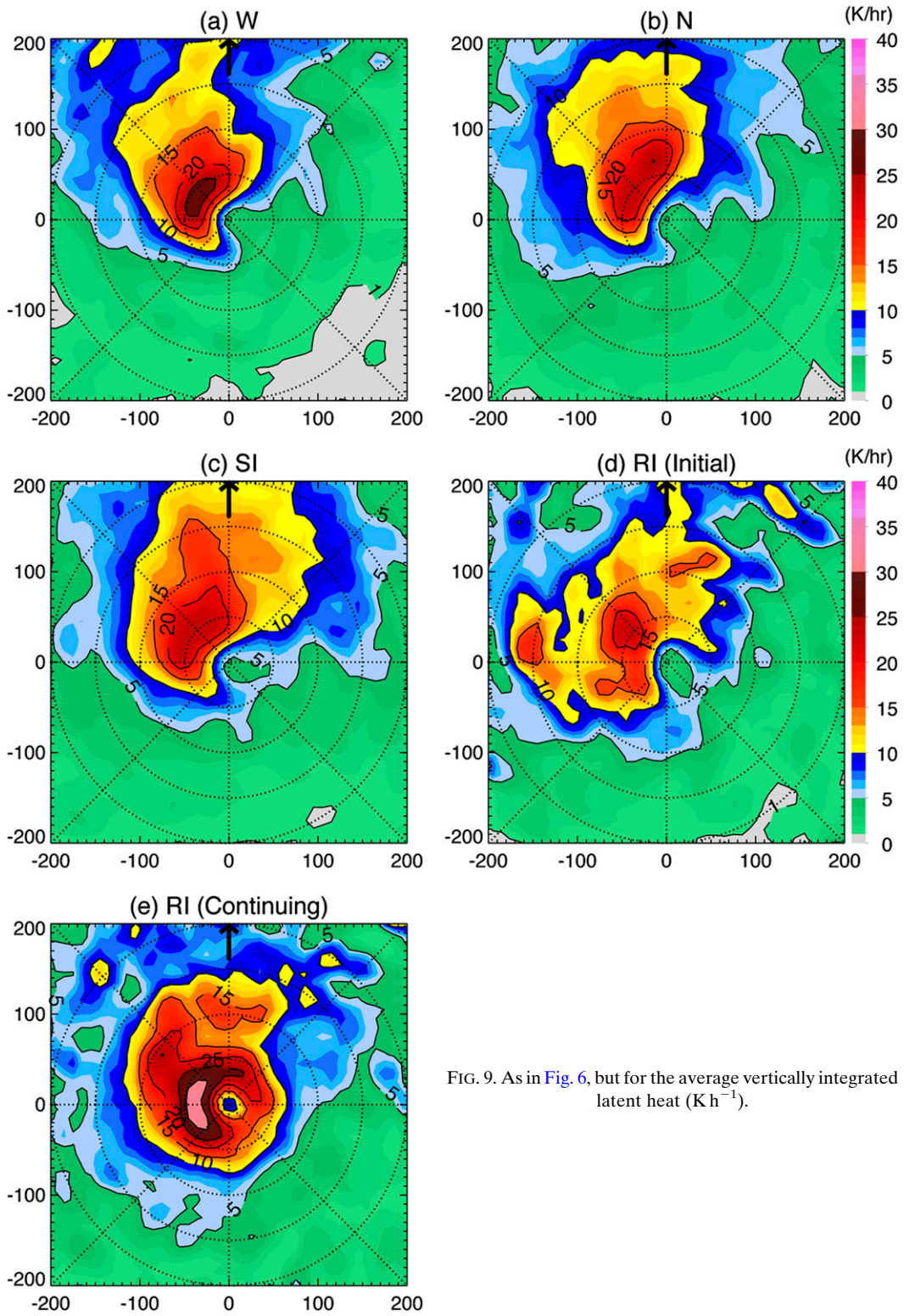
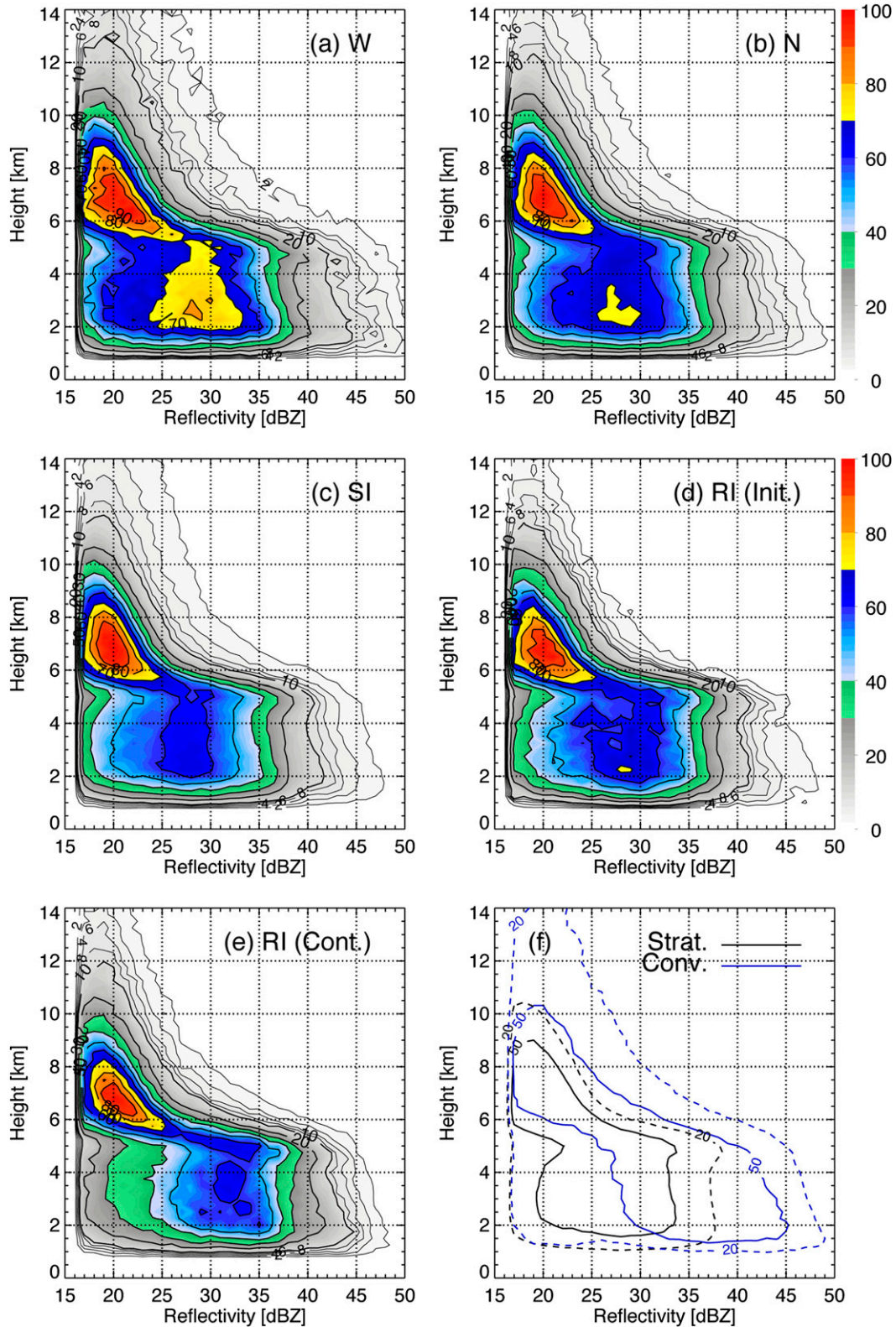FIG. 9. As in Fig. 6, but for the average vertically integrated latent heat (K h^{-1}).

FIG. 10. (a)–(e) CFADs for the inner 75-km, upshear semicircle (UL and UR combined) in the five intensity change categories. Contours represent the frequency occurrence relative to the maximum frequency bin (1 dB in size, 250 m in height) in each CFAD. (f) The 50% (modal; solid) and 20% (dashed) contour for the PR 2A23 stratiform (black) and convective (blue) pixels from the full sample.
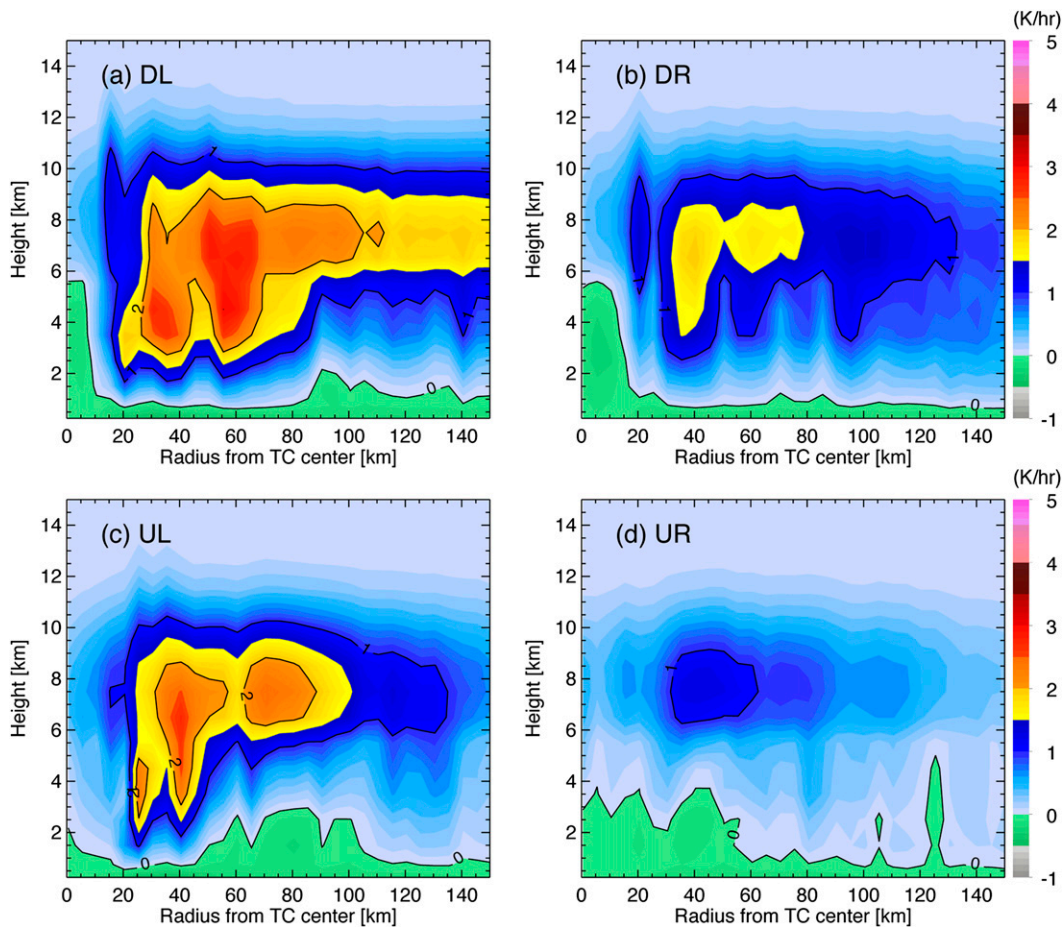
FIG. 11. Radial–height diagrams of latent heating (K h^{-1}) for RI (initial) storms only. Data are separated by shear-relative quadrants into (a) DL, (b) DR, (c) UL, and (d) UR.

distribution for RI (continuing) storms is shown in Fig. 12. The contours represent the average latent heating in each shear-relative quadrant relative to height and distance from the TC center. Areas with deep latent heating from 2 to 10 km are composed of primarily convective precipitation, while areas with latent heating concentrated above the approximate 5-km freezing level are stratiform dominant. An improved version of the LH algorithm would likely include additional cooling (negative latent heating) near the surface below the convective areas (Park and Elsberry 2013). The PR 2A23 stratiform-convective algorithm confirms these general divisions, as the percentage of LH derived from convective pixels in Figs. 11 and 12 combined is 71% in the 25–50-km annulus compared with 45% in the 75–100-km annulus. It is possible to generate similar radial–height diagrams for mean reflectivity, which is a more direct measure of the storm and less likely to be biased than the LH algorithm. However, the differences in mean reflectivity are more subtle because the increased coverage of precipitation is a much

greater factor in explaining the SI − RI LH differences than the intensity of the convection that is present.

The RI (initial) radial height diagram (Fig. 11) shows the expected downshear left dominant latent heating distribution, similar to the radar reflectivity distributions in Black et al. (2002), Hence and Houze (2011, 2012), and Reasor et al. (2013). The areas of deepest latent heat release are generally within the innermost 50–75 km of the center, with the profiles taking on a more stratiform appearance in the inner-rainband region beyond 100 km. The SI diagram (not pictured) looks remarkably similar to Fig. 11. The RI (continuing) latent heating (Fig. 12) has greater latent heating in all four quadrants, but is especially noteworthy because the strongest and deepest latent heating is concentrated within the innermost 50 km in all four quadrants. The downshear-left LH profiles peak at the 3–8-km elevation, which suggests a predominantly deep convective LH profile (Schumacher et al. 2004). The upshear-left peak is still convective, but it does not extend quite as high as downshear left,
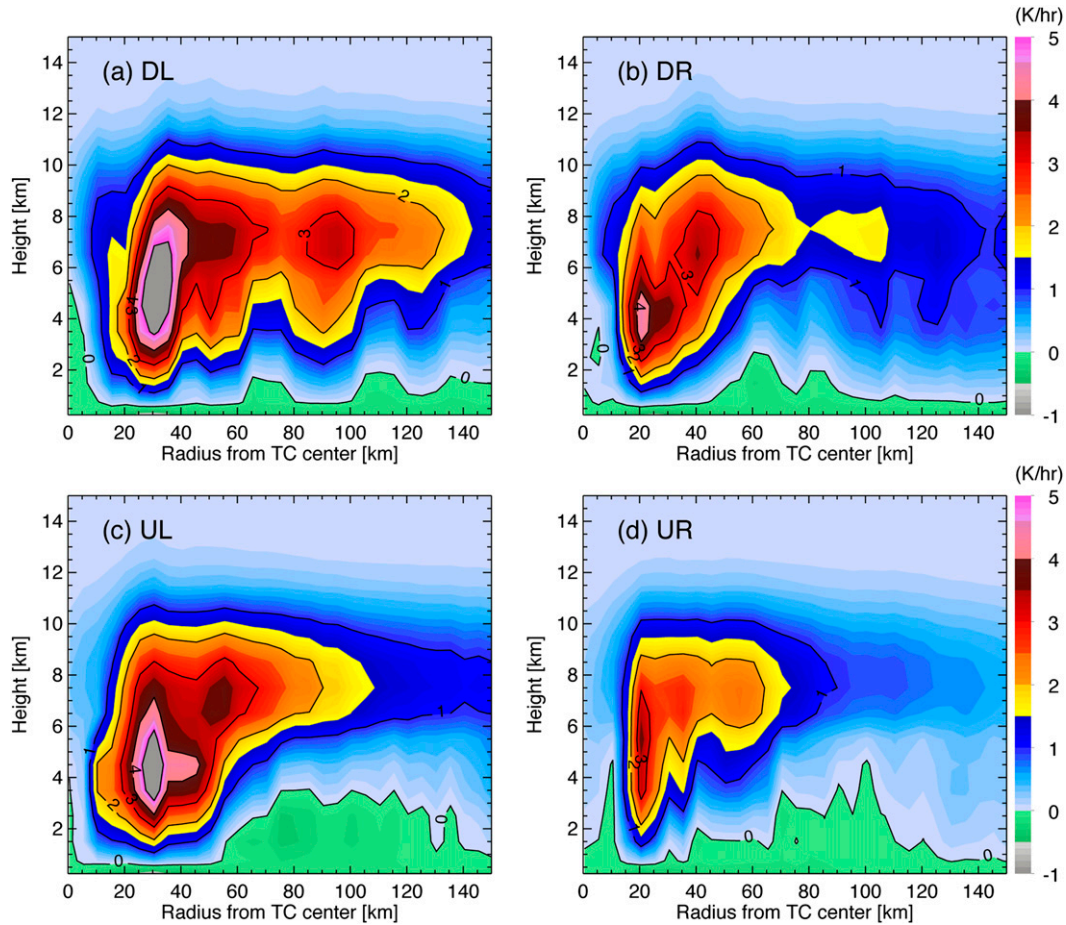
FIG. 12. As in Fig. 10, but for the RI (continuing) storms.

indicating weaker convection upshear. These radial height diagrams are remarkably consistent with the RI model simulation in Rogers (2010). In his study, the inner-core precipitation evolves from a mixture of convective and stratiform prior to RI to predominately convective after RI has begun. If the evidence from the PR is indeed analogous to the modeled updraft mass fluxes, then it is likely that on the convective scale, RI is first manifested as an increase in the low-level mass flux from weak to moderate convective updrafts.

e. Assessing variation in the dataset

The greatest limitation of the composite analysis is that it does not give any information about the specific behavior of any given storm. This section presents some statistical analysis in order to further assess the potential of each parameter to improve statistical RI forecasts. In this section, each data point represents a rainfall or convective coverage value for an individual TC as opposed to a frequency value from the combination of multiple TCs in the composite images. The scatterplot in

Fig. 13 shows the scatterplots of inner 75-km rainfall, convective, and latent heating coverage relative to the future 24-h intensity change. The bottom two panels show a simple asymmetry ratio, which is calculated by taking the highest inner 75-km rainfall coverage or latent heating value from the four shear-relative quadrants and dividing it by the mean. As in Table 3, the sample size is reduced to 559 after removing TRMM overpasses that miss more than a third of the inner 75 km. The coverage of PR reflectivity >20 dBZ (Fig. 13a) has the highest correlation coefficient relative to future intensity change (0.34). Weakening, neutral, and slowly intensifying storms have broad rainfall distributions raining from near zero rainfall frequency up to 95%. With the exception of two cases, rapidly intensifying storms have a minimum inner 75-km rainfall coverage around 25%, which is generally consistent with the finding in Jiang and Ramirez (2013) that inner-core rainfall coverage of at least 3000 km^2 is a necessary condition for RI. When rainfall coverage is above 50%, the probability of RI is 24%, compared with only 5%
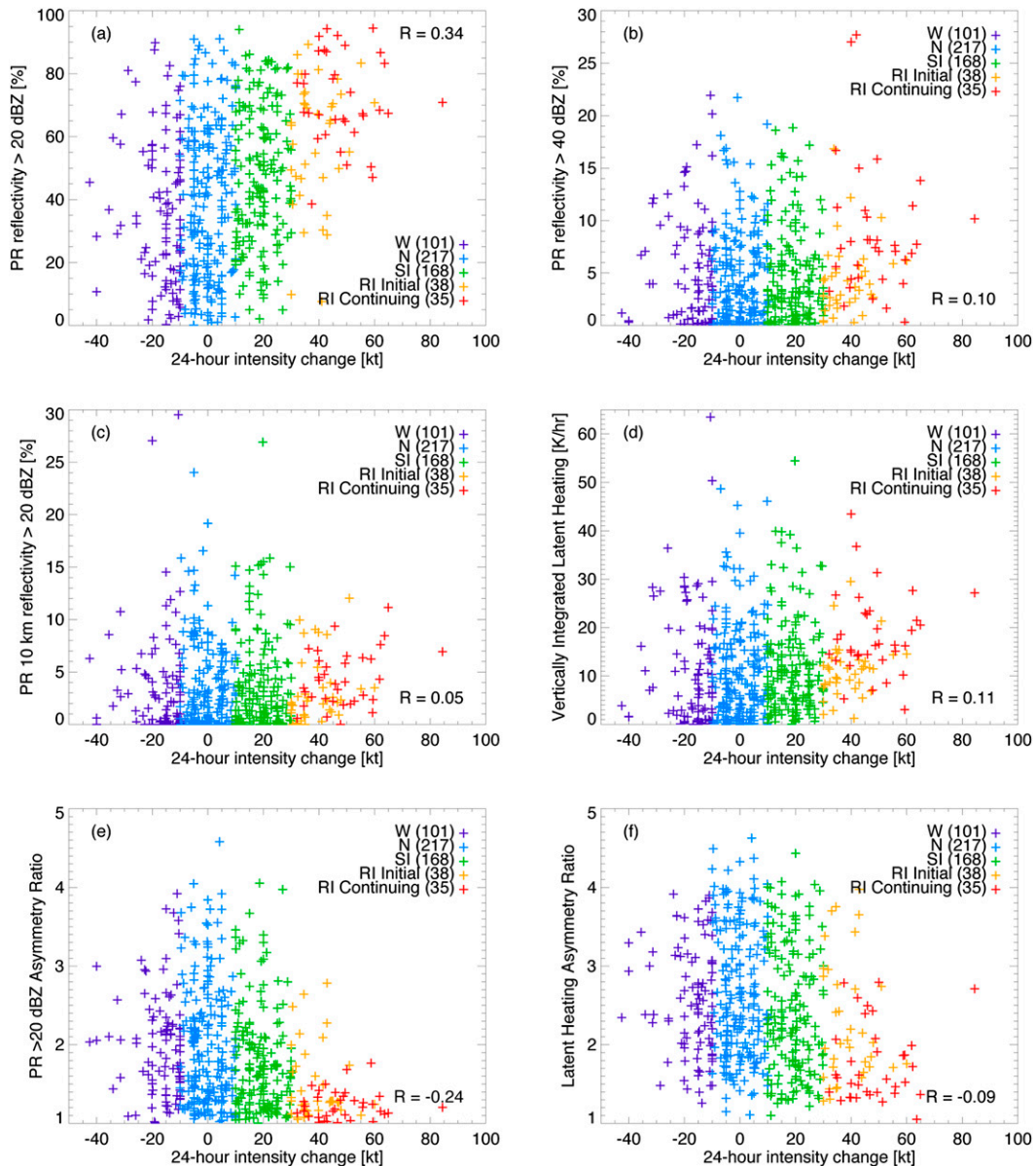
FIG. 13. Scatterplots of various (a)–(c) rainfall and (d) convective parameters (in the innermost 75 km) relative to the intensity change between the time of the TRMM overpass and 24 h later. (e),(f) The asymmetry ratio is defined as the maximum value divided by the inner 75-km mean. The correlation coefficient of the full sample (559 storms) is included in the bottom right [upper right in (a)].

when rainfall frequency is below 50%. In Fig. 13e, rainfall coverage also tends to be more symmetric (closer to one) in RI storms than other categories, although a large number of N and SI storms also have symmetric inner cores. The LH asymmetry ratio is not as strongly correlated with future intensity change, but as in Table 3, the RI (initial) and RI (continuing) storms are appreciably more symmetric.

Table 4 displays the mean values from the scatterplots. The mean difference in rainfall frequency (>20-dBZ

reflectivity frequency) between SI and RI (initial) is around 10% and is significant at the 99% confidence level. None of the other parameters are statistically significant between SI and RI (initial). The rainfall frequency between RI (initial) and RI (continuing) is also statistically significant. Since PR overpasses are rarely useful in operational forecasting, the rainfall coverage from the 37-GHz microwave imagery is the best way to apply this finding to operational intensity forecasts. The frequency of >40-dBZ reflectivity, LH, and both

asymmetry ratios are also statistically significant between RI (initial) and RI (continuing). The 10-km reflectivity parameter becomes meaningful (95% confidence level) if the sample is restricted to the inner 50 km, but the scatterplot in Fig. 13c shows almost no relationship between future intensity change and moderate-to-deep convection. This is not surprising because RI (continuing) cases do not necessarily have higher 24-h intensity change than RI (initial) storms, and therefore both RI (initial) and RI (continuing) cases fall within the same 24-h intensity change range in the x axis of Fig. 13. Although there is a significant difference of convective frequency (percentage of 10-km reflectivity >20 dBZ) between RI (initial) and RI (continuing), the difference between RI (initial) and SI is very small and insignificant. To have a significant relationship in Fig. 13c, a significant difference between all RI (including RI initial and continuing) and SI cases is needed, which is not what we see from Table 4.

4. Discussion

The PR rainfall distributions in this study have a close relationship to the 37-GHz precipitative ring (Kieper and Jiang 2012). Not all of the rapidly intensifying storms in this study have precipitating rings that match the requirement of at least a 90% closed ring around the TC center, which partially explains why the maximum rainfall frequency in the upshear-right quadrant in Fig. 6 is around 50% for RI (initial) and 75% for RI (continuing). Forecasting the 37-GHz ring is best accomplished by considering the initial and continuing RI periods as a single, continuous RI event. As noted in Kieper and Jiang (2012), the ring often does not appear at the onset of the RI event and is more effective at capturing the maximum period of 24-h RI, which is more closely analogous to the RI (continuing) than the RI (initial) category in this study. Specifically, the appearance of a 37-GHz ring was associated with the highest 24-h intensity increase in 16 out of the 23 RI events in Kieper and Jiang (2012). Therefore, it is not surprising that the greater and more symmetrical rainfall coverage in the RI (continuing) category is associated with an average 24-h intensity increase of 49 kt, compared with 39 kt for RI (initial). Another factor is the difference between the TRMM PR and the various microwave imagers used to detect the ring. The 37-GHz footprint is several times larger than the PR, so the shallow showers and convective cells that dominate the right-of-shear semicircle often only yield partial rainfall coverage at the PR resolution while appearing as part of the cyan colored ring in the 37-GHz color imagery. The PR also has a minimum reflectivity threshold around 17–18 dBZ, which adds further uncertainty for very light rain. The

upshear-right quadrant is the last quadrant to fill in with rainfall when the ring closes, so if a partial ring is present, the upshear-right quadrant is likely the open one. Additionally, the 37-GHz ring does not require a symmetric convective distribution. The main advantage of the 37-GHz channel is that it separates the primarily liquid/shallow (cyan) and frozen/deep (pink) convection. Moderate-to-deep convection clearly favors the left-of-shear side of the storm (Fig. 8), which corresponds in the 37-GHz imagery to a greater occurrence of pink on the left-of-shear side and a greater occurrence of cyan from the shallower convection that prevails in the right-of-shear side. This topic will be further examined in an upcoming article.

To more completely understand the processes leading to RI, it is important to consider how the rainfall and convective information from this study is related to changes in the TC vortex as RI unfolds. Since there is no observed increase in >10-km reflectivity of >20 dBZ between SI and RI (initial) storms, it does not appear that deep convection has an appreciable role in the onset of RI. Increased moderate-to-deep convection appears after RI has already been ongoing for ≥12 h, but the statistical distribution of reflectivity in the RI (continuing) CFAD (Fig. 10e) suggests the majority of the convection remains predominantly weak in nature. Rogers (2010) and Rogers et al. (2013) reached similar conclusions about convective bursts, although the bursts that do develop are preferentially located within the RMW in intensifying cases. The increase in deep convection within the RMW may be a positive feedback in response to changes in the vortex structure that enhance low-level convergence within the RMW (Rogers et al. 2013).

The rainfall frequency has higher value as an RI predictor compared with deep convection because, on average, rainfall becomes progressively more widespread in SI, RI (initial), and RI (continuing) storms. Oscillating convective activity means that a series of instantaneous satellite overpasses may observe the convection in different stages (e.g., developing, mature, and dissipating). Deep convective bursts are temporary features and only have a lifetime of a few hours (Heymsfield et al. 2001). The near-surface reflectivity >20-dBZ parameter captures the convection in all stages, so it considers areas of young or shallow convection that may eventually develop into deeper eyewall convection later in the RI process. Broader rainfall coverage also signifies a relatively moist lower and middle troposphere, which lessens the strength and frequency of negatively buoyant downdrafts from suppressing future convection (Riemer and Montgomery 2011; Molinari et al. 2013). The result is that a greater and steady supply of latent heat release is available for continued strengthening.

Factors such as decreasing vertical wind shear leading to lessened vertical vortex tilting (DeMaria 1996) are likely important as well. While it is known from observations of 37-GHz precipitative ring (Kieper and Jiang 2012) that increased rainfall coverage combined with favorable environmental conditions greatly increases the probability of RI, the details are still uncertain regarding the development of additional rainfall prior to and in the early stages of RI, especially in the upshear quadrants. The CFADs in Fig. 10 indicate that increased upshear precipitation is mostly from new convective development as opposed to broadening stratiform regions associated with older convective cells. The vortex-scale processes associated with this transition are likely important for understanding the processes that lead to the onset and continuation of RI.

5. Conclusions

The TRMM PR reflectivity data indicate that when at least moderately favorable environmental conditions exist, the frequency of near-surface >20-dBZ echoes are most strongly correlated with future intensity change. On average, TCs near the beginning of RI do not necessarily have the strongest or most widespread deep convection in the inner core. Tropical cyclones that have already been undergoing RI for at least 12 h have about 50% more moderate-to-deep convection than initially rapidly intensifying storms in the critical 25–50-km annulus (near or within the RMW) where convection is most efficient at strengthening the vortex (Fig. 5c). The higher rainfall frequency and latent heat release upshear of the TC center (Figs. 6d,e, 7b,c, 9d,e, and 12c,d) suggest a moist, high-entropy environment with lesser downdrafts and a greater frequency of weak convective and stratiform rain (Figs. 10d,e). The rainfall frequency and LH distributions are more symmetric in both the RI (initial) and especially the RI (continuing) categories as precipitation fills in the upshear quadrants. A related study using TRMM microwave imagery will address the differences between basins and better compare these results to the 37-GHz precipitative ring. More details on the TC vortex are needed as well, which would best be provided by airborne Doppler radar observations prior to and during RI. Alternatively, it may be possible to restructure some of the TRMM data relative to RMW estimates from other sources.

REFERENCES

Awaka, J., T. Iguchi, and K. Okamoto, 2009: TRMM PR standard algorithm 2A23 and its performance on bright band detection. *J. Meteor. Soc. Japan,* **87,** 31–52, doi:10.2151/jmsj.87A.31.

Black, M. L., J. F. Gamache, F. D. Marks, C. E. Samsury, and H. E. Willoughby, 2002: Eastern Pacific hurricanes Jimena of 1991 and Olivia of 1994: The effect of vertical shear on structure and intensity. *Mon. Wea. Rev.,* **130,** 2291–2312, doi:10.1175/1520-0493(2002)130<2291:EPHJOA>2.0.CO;2.

Cecil, D. J., and E. J. Zipser, 1999: Relationships between tropical cyclone intensity and satellite-based indicators of inner core convection: 85-GHz ice-scattering signature and lightning. *Mon. Wea. Rev.,* **127,** 103–123, doi:10.1175/1520-0493(1999)127<0103:RBTCIA>2.0.CO;2.

——, ——, and S. W. Nesbitt, 2002: Reflectivity, ice scattering, and lightning characteristics of hurricane eyewalls and rainbands. Part I: Quantitative description. *Mon. Wea. Rev.,* **130,** 769–784, doi:10.1175/1520-0493(2002)130<0769:RISALC>2.0.CO;2.

Chen, S. S., J. A. Knaff, and F. D. Marks, 2006: Effects of vertical wind shear and storm motion on tropical cyclone rainfall asymmetries deduced from TRMM. *Mon. Wea. Rev.,* **134,** 3190–3208, doi:10.1175/MWR3245.1.

Corbosiero, K. L., and J. Molinari, 2003: The relationship between storm motion, vertical wind shear, and convective asymmetries in tropical cyclones. *J. Atmos. Sci.,* **60,** 366–376, doi:10.1175/1520-0469(2003)060<0366:TRBSMV>2.0.CO;2.

DeHart, J. C., R. A. Houze Jr., and R. F. Rogers, 2014: Quadrant distribution of tropical cyclone inner-core kinematics in relation to environmental shear. *J. Atmos. Sci.,* **71,** 2713–2732, doi:10.1175/JAS-D-13-0298.1.

DeMaria, M., 1996: The effect of vertical shear on tropical cyclone intensity change. *J. Atmos. Sci.,* **53,** 2076–2088, doi:10.1175/1520-0469(1996)053<2076:TEOVSO>2.0.CO;2.

Hence, D. A., and R. A. Houze Jr., 2011: Vertical structure of hurricane eyewalls as seen by the TRMM Precipitation Radar. *J. Atmos. Sci.,* **68,** 1637–1652, doi:10.1175/2011JAS3578.1.

——, and ——, 2012: Vertical structure of tropical cyclone rainbands as seen by the TRMM Precipitation Radar. *J. Atmos. Sci.,* **69,** 2644–2661, doi:10.1175/JAS-D-11-0323.1.

Hendricks, E. A., M. S. Peng, B. Fu, and T. Li, 2010: Quantifying environmental control on tropical cyclone intensity change. *Mon. Wea. Rev.,* **138,** 3243–3271, doi:10.1175/2010MWR3185.1.

Heymsfield, G. M., J. B. Halverson, J. Simpson, L. Tian, and T. P. Bui, 2001: ER-2 Doppler Radar investigations of the eyewall of Hurricane Bonnie during the Convection and Moisture Experiment-3. *J. Appl. Meteor.,* **40,** 1310–1330, doi:10.1175/1520-0450(2001)040<1310:EDRIOT>2.0.CO;2.

Jiang, H., 2012: The relationship between tropical cyclone intensity change and the strength of inner-core convection. *Mon. Wea. Rev.,* **140,** 1164–1176, doi:10.1175/MWR-D-11-00134.1.

——, and E. M. Ramirez, 2013: Necessary conditions for tropical cyclone rapid intensification as derived from 11 years of TRMM data. *J. Climate,* **26,** 6459–6470, doi:10.1175/JCLI-D-12-00432.1.

——, C. Liu, and E. J. Zipser, 2011: A TRMM-based tropical cyclone cloud and precipitation feature database. *J. Appl. Meteor. Climatol.,* **50,** 1255–1274, doi:10.1175/2011JAMC2662.1.

Kaplan, J., and M. DeMaria, 2003: Large-scale characteristics of rapidly intensifying tropical cyclones in the North Atlantic basin. *Wea. Forecasting,* **18,** 1093–1108, doi:10.1175/1520-0434(2003)018<1093:LCORIT>2.0.CO;2.

——, ——, and J. A. Knaff, 2010: A revised tropical cyclone rapid intensification index for the Atlantic and eastern North Pacific basins. *Wea. Forecasting,* **25,** 220–241, doi:10.1175/2009WAF2222280.1.

Kieper, M., and H. Jiang, 2012: Predicting tropical cyclone rapid intensification using the 37 GHz ring pattern identified from passive microwave measurements. *Geophys. Res. Lett.,* **39,** L13804, doi:10.1029/2012GL052115.

Kummerow, C., W. Barnes, T. Kozu, J. Shiue, and J. Simpson, 1998: The Tropical Rainfall Measuring Mission (TRMM) sensor package. *J. Atmos. Oceanic Technol.,* **15,** 809–817, doi:10.1175/1520-0426(1998)015<0809:TTRMMT>2.0.CO;2.

Lee, T. F., F. J. Turk, J. Hawkins, and K. Richardson, 2002: Interpretation of TRMM TMI images of tropical cyclones. *Earth Interact.,* **6,** doi:10.1175/1087-3562(2002)006<0001:IOTTIO>2.0.CO;2.

Molinari, J., and D. Vollaro, 2010: Rapid intensification of a sheared tropical storm. *Mon. Wea. Rev.,* **138,** 3869–3885, doi:10.1175/2010MWR3378.1.

——, P. Dodge, D. Vollaro, K. L. Corbosiero, and F. Marks Jr., 2006: Mesoscale aspects of the downshear reformation of a tropical cyclone. *J. Atmos. Sci.,* **63,** 341–354, doi:10.1175/JAS3591.1.

——, J. Frank, and D. Vollaro, 2013: Convective bursts, downdraft cooling, and boundary layer recovery in a sheared tropical storm. *Mon. Wea. Rev.,* **141,** 1048–1060, doi:10.1175/MWR-D-12-00135.1.

Nesbitt, S. W., E. J. Zipser, and D. J. Cecil, 2000: A census of precipitation features in the tropics using TRMM: Radar, ice scattering, and lightning observations. *J. Climate,* **13,** 4087–4106, doi:10.1175/1520-0442(2000)013<4087:ACOPFI>2.0.CO;2.

Nguyen, L. T., and J. Molinari, 2012: Rapid intensification of a sheared, fast-moving hurricane over the Gulf Stream. *Mon. Wea. Rev.,* **140,** 3361–3378, doi:10.1175/MWR-D-11-00293.1.

Nolan, D. S., and L. D. Grasso, 2003: Nonhydrostatic, three-dimensional perturbations to balanced, hurricane-like vortices. Part II: Symmetric response and nonlinear simulations. *J. Atmos. Sci.,* **60,** 2717–2745, doi:10.1175/1520-0469(2003)060<2717:NTPTBH>2.0.CO;2.

——, Y. Moon, and D. P. Stern, 2007: Tropical cyclone intensification from asymmetric convection: Energetics and efficiency. *J. Atmos. Sci.,* **64,** 3377–3405, doi:10.1175/JAS3988.1.

Park, M.-S., and R. L. Elsberry, 2013: Latent heating and cooling rates in developing and nondeveloping tropical disturbances during TCS-08: TRMM PR versus ELDORA retrievals. *J. Atmos. Sci.,* **70,** 15–35, doi:10.1175/JAS-D-12-083.1.

Pendergrass, A. G., and H. E. Willoughby, 2009: Diabatically induced secondary flows in tropical cyclones. Part I: Quasi-steady forcing. *Mon. Wea. Rev.,* **137,** 805–821, doi:10.1175/2008MWR2657.1.

Reasor, P. D., M. D. Eastin, and J. F. Gamache, 2009: Rapidly intensifying Hurricane Guillermo (1997). Part I:

Low-wavenumber structure and evolution. *Mon. Wea. Rev.,* **137,** 603–631, doi:10.1175/2008MWR2487.1.

——, R. Rogers, and S. Lorsolo, 2013: Environmental flow impacts on tropical cyclone structure diagnosed from airborne Doppler radar composites. *Mon. Wea. Rev.,* **141,** 2949–2969, doi:10.1175/MWR-D-12-00334.1.

Reynolds, R. W., T. M. Smith, C. Liu, D. B. Chelton, K. S. Casey, and M. G. Schlax, 2007: Daily high-resolution-blended analyses for sea surface temperature. *J. Climate,* **20,** 5473–5496, doi:10.1175/2007JCLI1824.1.

Riemer, M., and M. Montgomery, 2011: Simple kinematic models for the environmental interaction of tropical cyclones in vertical wind shear. *Atmos. Chem. Phys.,* **11,** 9395–9414, doi:10.5194/acp-11-9395-2011.

Rogers, R., 2010: Convective-scale structure and evolution during a high-resolution simulation of tropical cyclone rapid intensification. *J. Atmos. Sci.,* **67,** 44–70, doi:10.1175/2009JAS3122.1.

——, P. Reasor, and S. Lorsolo, 2013: Airborne Doppler observations of the inner-core structural differences between intensifying and steady-state tropical cyclones. *Mon. Wea. Rev.,* **141,** 2970–2991, doi:10.1175/MWR-D-12-00357.1.

Schubert, W. H., and J. J. Hack, 1982: Inertial stability and tropical cyclone development. *J. Atmos. Sci.,* **39,** 1687–1697, doi:10.1175/1520-0469(1982)039<1687:ISATCD>2.0.CO;2.

Schumacher, C., R. A. Houze Jr., and I. Kraucunas, 2004: The tropical dynamical response to latent heating estimates derived from the TRMM Precipitation Radar. *J. Atmos. Sci.,* **61,** 1341–1358, doi:10.1175/1520-0469(2004)061<1341:TTDRTL>2.0.CO;2.

Shige, S., Y. N. Takayabu, W.-K. Tao, and D. E. Johnson, 2004: Spectral retrieval of latent heating profiles from TRMM PR data. Part I: Development of a model-based algorithm. *J. Appl. Meteor.,* **43,** 1095–1113, doi:10.1175/1520-0450(2004)043<1095:SROLHP>2.0.CO;2.

——, ——, ——, and C.-L. Shie, 2007: Spectral retrieval of latent heating profiles from TRMM PR data. Part II: Algorithm improvement and heating estimates over tropical ocean regions. *J. Appl. Meteor. Climatol.,* **46,** 1098–1124, doi:10.1175/JAM2510.1.

Simmons, A., S. Uppala, D. Dee, and S. Kobayashi, 2006: ERA-Interim: New ECMWF reanalysis products from 1989 onwards. *ECMWF Newsletter,* No. 110, ECMWF, Reading, United Kingdom, 26–35.

Sitkowski, M., and G. M. Barnes, 2009: Low-level thermodynamic, kinematic, and reflectivity fields of Hurricane Guillermo (1997) during rapid intensification. *Mon. Wea. Rev.,* **137,** 645–663, doi:10.1175/2008MWR2531.1.

Spencer, R. W., H. M. Goodman, and R. E. Hood, 1989: Precipitation retrieval over land and ocean with the SSM/I: Identification and characteristics of the scattering signal. *J. Atmos. Oceanic Technol.,* **6,** 254–273, doi:10.1175/1520-0426(1989)006<0254:PROLAO>2.0.CO;2.

Vigh, J. L., and W. H. Schubert, 2009: Rapid development of the tropical cyclone warm core. *J. Atmos. Sci.,* **66,** 3335–3350, doi:10.1175/2009JAS3092.1.

Willoughby, H. E., J. A. Clos, and M. B. Shoreibah, 1982: Concentric eye walls, secondary wind maxima, and the evolution of the hurricane vortex. *J. Atmos. Sci.,* **39,** 395–411, doi:10.1175/1520-0469(1982)039<0395:CEWSWM>2.0.CO;2.

Yuter, S. E., and R. A. Houze, 1995: Three-dimensional kinematic and microphysical evolution of Florida cumulonimbus: Part II: Frequency distributions of vertical velocity, reflectivity, and differential reflectivity. *Mon. Wea. Rev.,* **123,** 1941–1963, doi:10.1175/1520-0493(1995)123<1941:TDKAME>2.0.CO;2.